Editors' Suggestion

Intrinsic Carrier Mobility of Cesium Lead Halide Perovskites

Youngho Kang[1,*] and Seungwu Han[2]

[1] *Materials Data Center, Korea Institute of Materials Science, Changwon 51508, Korea*

[2] *Department of Materials Science and Engineering and Research Institute of Advanced Materials, Seoul National University, Seoul 08826, Korea*

(Received 23 May 2018; revised manuscript received 22 July 2018; published 4 October 2018)

Inorganic cesium-lead-halide perovskites ($CsPbX_3$, where X = Cl, Br, and I) have recently emerged as promising semiconductors for photovoltaic and light-emitting devices. In this study, we investigate electronic and vibrational properties of $CsPbX_3$ using the density-functional-theory calculations. We explicitly evaluate **k**-dependent electron-phonon scattering rates of the polar longitudinal-optical phonon modes. The transport property at room temperature is then computed based on Boltzmann transport theory within the relaxation-time approximation. The computational results identify the fundamental limit of the carrier mobility and its dependence on the halide species. Our results show that different choices of X lead to the variation in the mobility by a factor of 3 to 5 depending on the carrier concentration between 10^{15} and 10^{18} cm^{-3}. The preferred carrier type (electron or hole) in terms of the mobility also varies with X. Through the detailed analysis on the band structures and scattering rates, we provide insights into the role of halide species in the transport properties.

DOI: 10.1103/PhysRevApplied.10.044013

I. INTRODUCTION

Organic-inorganic hybrid lead-halide perovskites with a chemical formula of $APbX_3$, where A is an organic cation and X is Cl, Br, and I, have emerged as semiconductors that may lead to a breakthrough in photovoltaic (PV) devices [1,2]. The power conversion efficiency (PCE) of the PV cell based on $APbX_3$ has improved in a spectacular way over the past few years, exceeding 20% as of now [3]. In addition, $APbX_3$ has exhibited high photoluminescence quantum efficiency (PQE) [2], triggering active research studies toward light-emitting devices. However, the organic-inorganic hybrid perovskites have stability issues under ambient conditions, posing a critical hurdle against actual commercialization [2,4]. Since this instability stems from mainly A-site organic cations, attention is being directed toward developing all-inorganic lead-halide perovskites [5–12].

The cesium-lead-halide perovskite ($CsPbX_3$) is attracting increasing attention owing to outstanding optoelectrical properties and good stability. It has been demonstrated that the device performance of $CsPbX_3$ is as high as those of hybrid perovskites, while the device stability has improved significantly [4,10,11]. Despite growing interest, understanding on the fundamental properties $CsPbX_3$ is still insufficient. In particular, the carrier transport properties, which limit the current characteristics of PV and light-emitting devices, have been poorly understood. For example, measured mobilities of single crystal samples are rather scattered over a wide range [approximately 10–1000 cm^2/Vs] [8–12]. In addition, the influence of halide elements on the transport properties, a route to tune the optical properties, has not been studied thoroughly.

Theoretically, the transport property of $CsPbX_3$ has been studied with various approaches. However, the calculated carrier mobility varies widely in the literature; electron (hole) mobilities for $CsPbI_3$ are 258 [13] and 74 (98) [14] cm^2/Vs and those for $CsPbBr_3$ are 48 (41) [15] and 679 (52) [16] cm^2/Vs. We note that every method involves empirical parameters within the model, which may undermine consistency among the computational results. This inconsistency in calculated mobilities indicates that a full-blown first-principles approach that does not involve any empirical parameter is in demand.

In this work, we theoretically investigate the electron-phonon scattering rates and mobility of $CsPbX_3$ (X = Cl, Br, and I), which are critical parameters affecting PCE and PQE, based on the electronic band structures and zone-center phonon frequencies obtained using the density-functional-theory (DFT) calculations. All the parameters for calculating the transport properties are obtained from first-principles calculations and, therefore, the present approach is fully *ab initio*. We focus on electron-phonon scattering by polar longitudinal-optical (LO) phonon modes that are the dominant scattering source in polar materials due to polarity and long-range character [17,18]. The coupling of an electron to the polar LO modes is described by the generalized Fröhlich model

*thehoya84@gmail.com

[17]. The room-temperature carrier mobility is then evaluated by Boltzmann transport theory within the relaxation-time approximation, providing the intrinsic limit of the mobility. It is found that different halide species vary the mobility by a factor of 3 to 5 depending on the carrier concentration (n_c) between 10^{15} and 10^{18} cm^{-3}. In addition, it is found that the preferred carrier type (electron vs. hole) in terms of the mobility depends on halide species. The detailed analysis on the band structure and scattering rates provides an in-depth understanding on the role of halide species in the transport properties.

II. METHODS

The first-principles calculations are performed using the Vienna *ab initio* simulation package (VASP) [19] with projector augmented waves (PAW) [20]. The cutoff energy for expanding the plane-wave basis is 300 eV and a $6 \times 6 \times 6$ Monkhorst-Pack mesh is chosen for the Brillouin-zone (BZ) sampling. The semicore Pb d state is treated as a valence state. Regarding the exchange-correlation energy functional, we employ the HSE06 hybrid functional with the default 25% mixing of the Fock-exchange energy [21]. This default value slightly underestimates the band gap, but yields the band dispersion similar to GW results, which is critical for the transport property [22].

CsPbX_3 is known to have various polymorphs depending on the temperature [23]. Here, we choose the high-temperature cubic phase for the simplicity of the computations. Nevertheless, we expect that our conclusions in this work can still be applied to the room-temperature orthorhombic phase because the electronic structure is similar between the two phases [24] even if the slight difference in the mobility can arise from different electron-phonon coupling (see Sec. III E). Since the HSE functional requires significant computational resources for phonon calculations, we adopt the PBE functional in evaluating zone-center phonon frequencies while the lattice parameters are fixed to the HSE results. The previous literature confirms the validity of this approach in predicting phonon frequencies [25,26]. We evaluate the frequency splitting between the polar LO and transverse-optical (TO) modes by considering Born effective charges and high-frequency dielectric constant ε_∞, as implemented in Phonopy [27].

III. RESULTS AND DISCUSSIONS

A. Physical properties

Figure 1(a) shows the unit cell of the cubic CsPbX_3 perovskite. Because of the different ionic radii of halides, the calculated lattice parameters decrease as 6.33 Å(CsPbI$_3$) $>$ 5.95 Å(CsPbBr$_3$) $>$ 5.67 Å(CsPbCl$_3$), which is in good agreement with experiments [9,28,29]. The unit cell includes five atoms, and so there are 15 phonon modes (3 acoustic and 12 optical). Among these modes, three

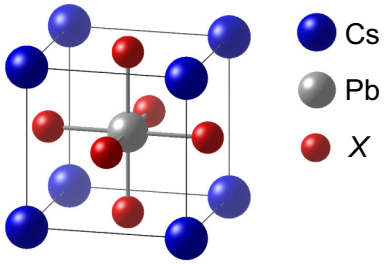

FIG. 1. The unit cell of the cubic CsPbX_3 perovskite.

groups of polar modes (two TO and one LO mode in each group) exist. We find that one group of the lowest polar optical modes has an imaginary frequency at the zone center, which was also found in earlier calculations [30,31]. This instability implies the presence of a ferroelectric distortion, but x-ray measurements confirm the space group of $Pm\bar{3}m$ [9]. Marronnier *et al.* have suggested that $Pm\bar{3}m$ may have resulted from the dynamic average among different ferroelectric configurations that exist over a smooth potential-energy surface [30]. This ferroelectric distortion is ignored in the present transport calculation because it does not affect the main conclusion, as will be discussed later.

In Table I, we list zone-center phonon frequencies (ω) of stable polar optical modes in cubic CsPbX_3. T(L)O$_1$ and T(L)O$_2$ denote the lower- and higher-frequency modes, respectively. It is seen that every frequency increases with a decreasing atomic number of X. This result is mainly a consequence of different lattice constants of CsPbX_3 because chemical bonds tend to be stronger in more compact structures, leading to higher phonon frequencies [25].

Figure 2 shows the band structures of CsPbX_3 plotted along the high symmetry points in the irreducible BZ. By inspecting the wave functions, we find that the hybridized states between Pb 6s and X np orbitals ($n = 3$, 4, and 5 for $X =$ Cl, Br, and I, respectively) form the valence-band top, while the conduction-band minimum is mainly contributed by the Pb 6p, X ns, and X np orbitals. It is also seen in Fig. 2 that degeneracy of the conduction bands is lifted at R due to the large spin-orbit coupling (SOC) of Pb [23].

The effective mass (m^*) at band edges along the R-Γ, R-X, and R-M directions is computed by fitting the band structure (with SOC) along each direction to the hyperbolic

TABLE I. Calculated zone-center frequencies of stable polar TO and LO modes, in units of meV, and high-frequency dielectric constant (ε_∞).

	ω_{TO_1}	ω_{TO_2}	ω_{LO_1}	ω_{LO_2}	ε_∞
CsPbCl$_3$	6.68	16.51	7.66	28.24	3.69
CsPbBr$_3$	4.82	11.66	5.62	19.42	4.30
CsPbI$_3$	3.42	9.80	4.53	15.52	5.26

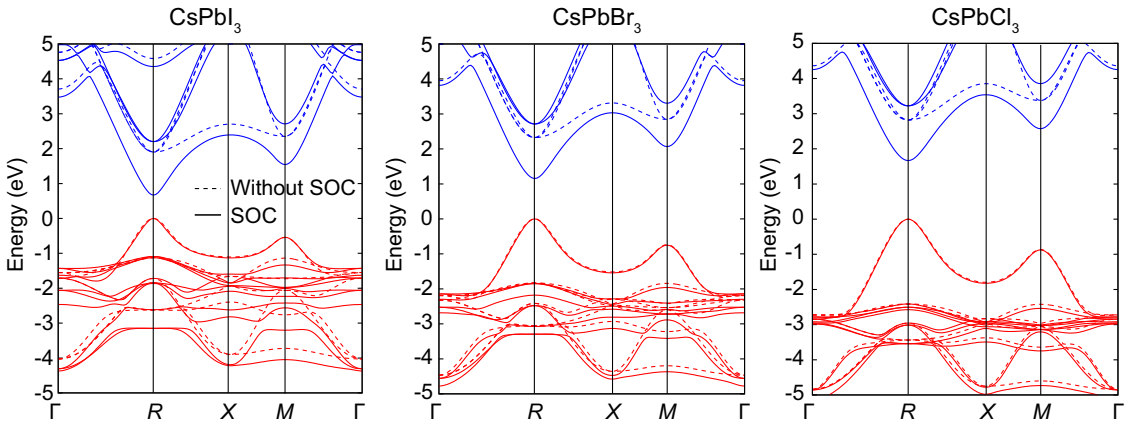

FIG. 2. Band structures of $CsPbX_3$ for X = I, Br, and Cl with or without spin-orbit coupling (SOC). The valence-band maximum at R is set to 0.

dispersion relation:

$$\frac{\hbar^2|\mathbf{k}|^2}{2m^*} = \epsilon_{\mathbf{k}}(1+\alpha\epsilon_{\mathbf{k}}), \tag{1}$$

where α is the nonparabolicity factor and $\epsilon_{\mathbf{k}}$ is the energy of the electronic state. We find that m^* has a weak anisotropy displaying the maximum 10% variation between different directions, consistent with previous calculations [32]. The small anisotropy in m^* indicates that the band dispersion near the band edges is fairly isotropic. On the other hand, α exhibits significant dependence on the directions. As a result, anisotropy in the band structures is amplified as $\mathbf{k}$ shifts away from R. For most applications of $CsPbX_3$, the carrier concentration is likely to be lower than 10^{18} cm^{-3}, meaning that the Fermi level lies close to the band edges [33]. Thus, to avoid complications in the transport analysis, we assume isotropic band structures represented by Eq. (1) with averaged parameters for m^* and α along the three high-symmetry directions (see Table II). Figure 3 compares the band dispersion around the conduction-band minimum of $CsPbI_3$, which shows that anisotropy is indeed weak and so the band dispersion can be approximated as an isotropic one.

In Table II, m^* becomes lighter with an increasing atomic number of X, irrespective of the type of carrier. This X dependence of m^* is associated with the energetic positions of the ns and np states of X that contribute to the formation of valence and conduction bands along with the Pb $5s$ and $5p$ states; the orbitals of X are higher in energy as n increases, being close to the Pb states. As a consequence, the hybridization between orbitals of X and Pb becomes more efficient with an increasing atomic number of X, leading to more dispersive band structures.

The electronic structure of $CsPbX_3$ has been investigated in previous calculations [32,34]. The authors of Ref. [34] calculated the band structure using the local density approximation (LDA) and reported the isotropic and small hole effective mass (0.12–0.14m_e, where m_e is the electron mass), which is in good agremeent with our calculations. However, their electron effective mass is heavier and highly anisotropic (0.20–0.23m_e for the R-Γ and 0.54–0.67m_e for the R-M direction) because of the absence of the SOC effects in their calculations. On the

TABLE II. Directionally averaged effective masses (m^* in units of electron mass) and nonparabolicity parameters (α in units of eV^{-1}).

	Electron		Hole	
	m^*	α	m^*	α
$CsPbCl_3$	0.218	0.767	0.189	0.701
$CsPbBr_3$	0.149	1.033	0.143	1.054
$CsPbI_3$	0.087	1.628	0.094	2.211

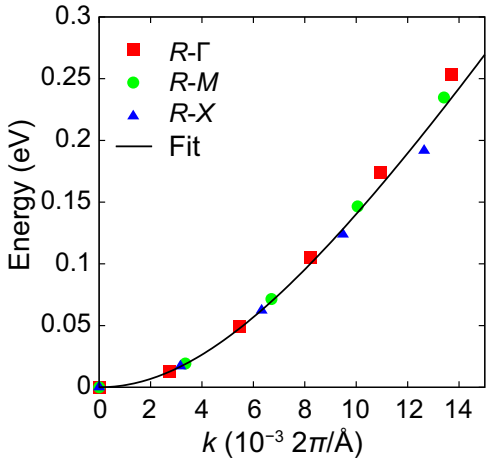

FIG. 3. Calculated dispersion of the lowest conduction band of $CsPbI_3$ along the R-Γ (red square), R-M (green circle), and R-X (blue triangle) directions. The black solid line shows the hyperbolic disperison [Eq. (1)] with parameters in Table II.

other hand, the authors of Ref. [32] computed the band diagram employing the hybrid functional with the SOC effects. Even if they also found the isotropic band dispersion, the absolute values of the effective mass in their calculations (0.2–0.4m_e for electron and $\sim 0.2m_e$ for hole) are larger than the present calculations. This discrepancy in m^* is attributed to different approaches to calculate the effective mass; we obtain the effective mass from the second derivative of the band dispersion, while it is estimated in Ref. [32] through transport calculations under the constant relaxation time.

B. Scattering rates

The **k**-dependent scattering rate ($\tau_{\mathbf{k}}^{-1}$) due to electron-phonon interactions is obtained from the Fermi golden rule as follows [35]:

$$\tau_{\mathbf{k}}^{-1} = \frac{2\pi}{\hbar}\sum_{\nu}\iiint_{\mathrm{BZ}}\frac{d\mathbf{q}}{8\pi^3}|g_{\mathbf{q}\nu}|^2(1-\hat{\mathbf{v}}_{\mathbf{k}}\cdot\hat{\mathbf{v}}_{\mathbf{k}+\mathbf{q}}) \times[(n_{\mathbf{q}\nu}+f_{\mathbf{k}+\mathbf{q}})\delta(\epsilon_{\mathbf{k}+\mathbf{q}}-\epsilon_{\mathbf{k}}-\hbar\omega_{\mathbf{q}\nu}) + (1+n_{\mathbf{q}\nu}-f_{\mathbf{k}+\mathbf{q}})\delta(\epsilon_{\mathbf{k}+\mathbf{q}}-\epsilon_{\mathbf{k}}+\hbar\omega_{\mathbf{q}\nu})], \quad (2)$$

where **q** and ν indicate the phonon wave vector and phonon mode, respectively, and $g_{\mathbf{q}\nu}$ is the matrix element for the electron-phonon coupling. $\hat{\mathbf{v}}_{\mathbf{k}}$ is the unit vector parallel to the group velocity ($\mathbf{v}_{\mathbf{k}}$) and $n_{\mathbf{q}\nu}$ and $f_{\mathbf{k}}$ are the Bose-Einstein and Fermi-Dirac distributions, respectively. In Eq. (2), the δ functions enforce the energy conservation when a phonon is absorbed or emitted. For the numerical integration, the δ functions are often replaced by smearing functions such as Gaussian or Lorentzian, but this approach requires extremely fine **q**-point grids to reach a good convergence [36]. Alternatively, we use the analytic form of the band dispersion in Eq. (1), which exactly determines the magnitude of **q** that satisfies the energy conservation. Thus, Eq. (2) can be evaluated by performing the integration with respect to two angular variables of **q** in the spherical coordinate without invoking δ functions. We also evaluate $\mathbf{v}_{\mathbf{k}}$ directly from the band dispersion:

$$\mathbf{v}_{\mathbf{k}} = \frac{1}{\hbar}\frac{\partial\epsilon_{\mathbf{k}}}{\partial\mathbf{k}}. \quad (3)$$

In Eq. 2, we omitted the band index, neglecting the interband scattering. This omission is reasonable because the band-edge states are well separated in energy from other bands, prohibiting interband transitions due to the electron-phonon scattering.

The electron-phonon matrix element for scattering by polar LO phonon modes can be calculated by the generalized Fröhlich model that is applicable to systems with an isotropic high-frequency dielectric constant and a vibrational spectrum, taking multiple optical phonon modes into account [17]:

$$|g_{\mathbf{q}\nu}|^2 = \frac{|\mathbf{q}|^2}{(|\mathbf{q}|^2+q_{\mathrm{scr}}^2)^2}\cdot\frac{e^2\hbar\omega_{\mathrm{LO},\nu}}{2\varepsilon_\infty\varepsilon_0 V_{\mathrm{cell}}} \times\frac{\prod_m\left(1-\frac{\omega_{\mathrm{TO},m}^2}{\omega_{\mathrm{LO},\nu}^2}\right)}{\prod_{m\neq\nu}\left(1-\frac{\omega_{\mathrm{LO},m}^2}{\omega_{\mathrm{LO},\nu}^2}\right)}, \quad (4)$$

where ε_0 and V_{cell} are the vacuum permittivity and the unit-cell volume, respectively, and q_{scr} is the wave vector for the free-carrier screening of the long-range potential. The high-frequency dielectric constants (ε_∞) for X = Cl, Br, and I are listed in Table I. Since the highly dispersive band structure of $CsPbX_3$ allows absorption or emission of phonons with only small wave vectors, phonon frequencies in Eq. 4 are effectively fixed to those at the zone center as shown in Table I.

Figure 4 shows the mode-resolved scattering rates in $CsPbI_3$ at the room temperature as a function of the energy for the electron carrier. The carrier density is set to 10^{18} cm^{-3}. It is noticeable that the LO_2 mode causes higher scattering rates than the LO_1 mode. This result is because $g_{\mathbf{q}\nu}$ tends to increase with the LO phonon frequency [see Eq. (4)]. This phenomenon is common to all $CsPbX_3$ systems. It is also seen in Fig. 4 that the scattering rates rise faster when the carrier energy crosses the phonon energy of LO modes as the phonon emission starts to contribute to the scattering mechanism.

We note that phonon frequencies in Table I are obtained at 0 K, so they can shift at finite temperatures due to anharmonicity or thermal expansion [37,38]. In compound semiconductors, the anharmonicity typically leads to frequency shifts of less than 1% when temperature increases

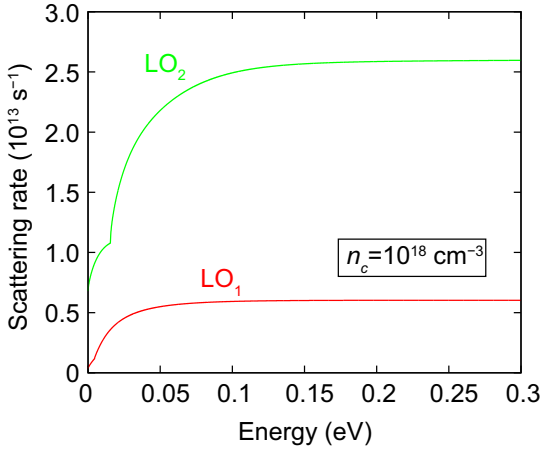

FIG. 4. Mode-resolved electron-phonon scattering rates for the electron carrier of $CsPbI_3$ at room temperature and $n_c = 10^{18}$ cm^{-3}. Energies of the x-axis are referenced to the conduction-band minimum.

from 0 to 300 K [38,39]. Therefore, anharmonic effects could be ignored in the electron transport calculations at room temperature. On the other hand, thermal expansion of the lattice parameter [9] affects phonon frequencies to some extent, which effectively enhances the scattering rate by approximately 10% according to the present estimation.

C. Mobility

Based on Boltzmann transport theory within the relaxation-time approximation, the carrier mobility μ at a given carrier density is calculated as follows [35]:

$$\mu = \frac{\sigma}{n_c e} = 2\frac{e}{N}\iiint_{\mathrm{BZ}} \frac{d\mathbf{k}}{8\pi^3}\tau_{\mathbf{k}}\left(-\frac{\partial f_{\mathbf{k}}}{\partial \epsilon_{\mathbf{k}}}\right) v_x^2, \qquad (5)$$

where σ is the conductivity. The factor of 2 on the right side accounts for the spin degree of freedom. Since $\partial f_{\mathbf{k}}/\partial\epsilon_{\mathbf{k}}$ peaks at the Fermi level, the conductivity is dictated by the carriers near the Fermi level. Since the mobility tensor is a scalar due to the cubic symmetry, we consider a specific direction in the velocity vector (x direction) in Eq. (5). The integration of Eqs. (2) and (5) is conducted numerically using the Matlab software package.

In Fig. 5, we present the room-temperature mobility as a function of the carrier concentration. It is found that the mobility in $CsPbX_3$ is nearly constant for low carrier densities ($n_c < 10^{17}$ cm^{-3}). This near-constant mobility is a result of effective cancellation of two competing factors, i.e., the group velocity and scattering rate. The magnitude of $\mathbf{v}_{\mathbf{k}}$ [or v_x^2 in Eq. (5)] in the vicinity of the Fermi level increases with the carrier concentration (or the Fermi level). At the same time, carriers are scattered more frequently, as shown in the energy-dependent scattering rates in Fig. 6. On the other hand, the scattering rate is rather saturated when the carrier energy becomes a few tens of meV above the onset of absorption of the highest LO modes. As

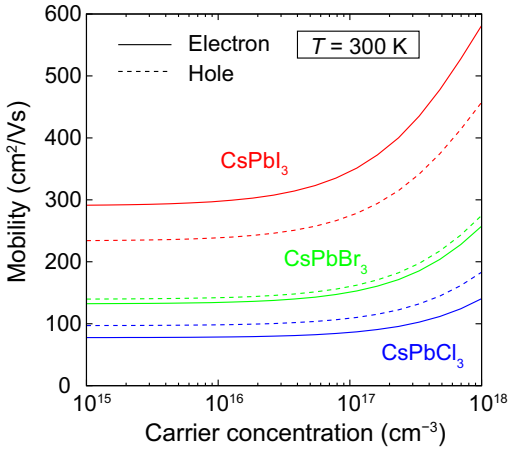

FIG. 5. Calculated electron and hole mobilities as a function of the carrier concentration at room temperature for $CsPbX_3$.

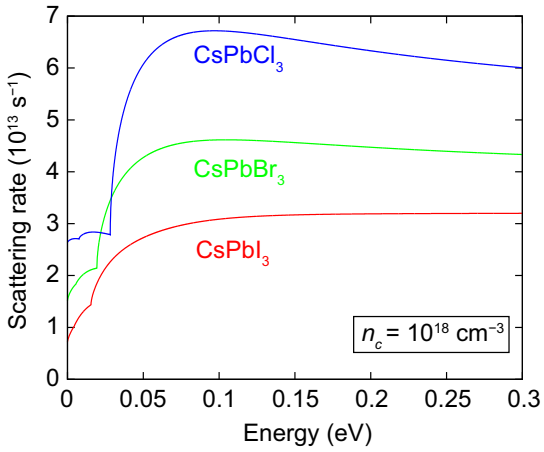

FIG. 6. Energy dependence of electron-phonon scattering rates for the electron carrier of $CsPbX_3$ at room temperature and $n_c = 10^{18}$ cm^{-3}. Energies of the x-axis are referenced to the conduction-band minimum.

a consequence, carriers experience almost the same scattering rates at high carrier densities, leading to the increase in mobility when the carrier concentration is bigger than 10^{17} cm^{-3}.

Figure 5 shows that the carrier mobility increases with the atomic number of halide species. Moreover, while in $CsPbI_3$ the electron mobility is higher than that of the hole, they are similar in $CsPbBr_3$ and reversed in $CsPbCl_3$. These results could be explained by invoking a simple Drude picture where the mobility is inversely proportional to the effective mass (see Table II). However, we note that the quantitative difference in the mobility is not fully accounted for by the mass difference alone. For instance, the electron mobility of $CsPbI_3$ is approximately 4 times higher than that of $CsPbCl_3$ at $n_c = 10^{18}$ cm^{-3}, but the effective mass is only approximately 2.5 times heavier. The remaining difference is associated with the scattering rates, which are higher in $CsPbX_3$ with lighter halide species, as shown in Fig. 6. The dependence of the scattering rate on the halide species is related to the density of states (DOS) near the Fermi level; a larger DOS raises the scattering rate by increasing the density of the final electronic states. Because DOS correlates positively with the effective mass, the scattering rates are higher in $CsPbCl_3$.

It would be worthwhile to compare the present results on the mobility with the previous calculations mentioned in the Introduction. Since the earlier works did not specify the carrier concentration, we assume their results correspond to the mobility at low carrier concentrations. We estimate the electron mobility of $CsPbI_3$ to be approximately 290 cm^2/Vs at room temperature and this result is similar to that in Ref. [13], which was obtained based on the Feynman polaron model. Regarding $CsPbBr_3$, the extant calculations deviate significantly from the present results (by more than

a factor of 3). We think that empirical parameters in those works need to be reexamined.

D. Effects of a ferroelectric distortion

In this subsection, we discuss potential effects of the ferroelectric distortion that arises from the instability of the lowest polar optical modes at the zone center. Marronnier *et al.* showed that displacing Cs and I slightly in the opposite direction stabilizes the soft modes in $CsPbI_3$, while it barely affects frequencies of the higher LO modes [30]. Using the frequencies of the lowest polar modes from phonon-band structures in Ref. [30], we examine its influence on the mobility. Since they did not label specific modes in the phonon spectra and other optical modes are present with similar frequencies, it is difficult to assign frequencies of the lowest LO-TO pair. As such, we select the minimum and maximum values of a frequency range (from 2.48 to 3.40 meV), where the pair is expected to exist, as frequencies of the lowest TO and LO modes, respectively. Because the matrix element in Eq. (4) increases with the LO-TO splitting, this choice represents the maximum possible scattering rate. Nevertheless, the calculation results show that the scattering of the lowest polar LO mode affects the mobility little, causing the reduction of the electron mobility of $CsPbI_3$ by only approximately 10%. This result is because of the weak electron-phonon coupling in comparison with other polar LO modes due to the lower frequency.

On the other hand, the electronic structure is also affected by the ferroelectric distortion. Because of the absence of the central symmetry in the distorted structure, Rashba splitting occurs in both conduction and valence bands. However, the Rashba effect causes only a small change in the band dispersion and, therefore, rarely influences the scattering rates and mobility [40].

E. Electron-phonon coupling in orthorhombic phase

We check the impacts of the orthorhombic lattice on the electron-phonon coupling and mobility, focusing on orthorhombic $CsPbBr_3$. As mentioned earlier, the generalized Fröhlich model [Eq. (4)] used to obtain the electron-phonon matrix elements in the cubic phase applies to isotropic systems. For anisotropic materials like orthorhombic $CsPbX_3$, more general approaches, e.g., explicit first-principles calculations or the Vogl model, are required to obtain the electron-phonon matrix elements. (For detailed information about various methodologies to calculate the electron-phonon coupling, we refer to Ref. [41].) However, we find that orthorhombic $CsPbBr_3$ ($a = 8.23$ Å, $b = 8.50$ Å, and $c = 11.87$ Å) has fairly isotropic high-frequency dielectric constants (4.17–4.39, depending on the crystal axis). Moreover, the anisotropy in its phonon dispersion around Γ is also found to be negligible [42], showing a weak dependence of phonon frequencies on the direction of **q**. Therefore, assuming that the vibrational spectrum is isotropic in the orthorhombic phase, we employ the generalized Fröhlich model for the electron-phonon matrix elements.

To compute the electron-phonon matrix elements in orthorhombic $CsPbBr_3$, we take the directional average of the high-frequency dielectric constants. The frequencies of polar LO and TO modes at the Γ point are needed to evaluate the matrix elements. Since they depend on the **q** direction, we test two sets of the LO-TO phonon frequencies at Γ: the first one is when **q** approaches Γ along the Γ-X and the other is along the Γ-Z lines. The two sets of frequencies result in the mobility of 109.4 and 111.7 cm^2/Vs at the room temperature and carrier concentration of 10^{15} cm^{-3}, respectively, which are similar to each other, as expected from the small anisotropy in the phonon dispersion. Those mobility values are comparable to 132.3 cm^2/Vs of the cubic phase. This can be explained in terms of the highest polar mode that gives the largest electron-phonon matrix elements and, hence, forms the dominant scattering channel; the frequency of the highest polar LO mode (approximately 17 meV) and the magnitude of the LO-TO splitting (approximately 6.5 meV) in the orthorhombic phase are comparable to those of the cubic phase (see Table I). Consequently, the impacts of the most relevant phonon mode on the scattering rate are similar in both phases.

F. Comparison with experiments and other calculations

For polycrystalline $CsPbI_3$ films, electron and hole mobilities of approximately 10–16 cm^2/Vs have been reported [6,7], which is an order of magnitude smaller than the theoretical estimation in the above. In experiment, the grain-boundary scattering may have limited the mobility significantly. One recent study measured the hole mobility of a single crystal $CsPbBr_3$ to be 143 cm^2/Vs [12], which is in favorable agreement with the calculated value. However, as mentioned in the Introduction, the experimental mobility for single crystal samples exhibits a wide range of values [approximately 10–1000 cm^2/Vs]. The systematic or statistical errors related to different measurement techniques may contribute to such scattered data [43]. We expect that the experimental mobility will eventually converge to the theoretical values via systematic transport measurements on single crystal samples.

The transport properties of organic-inorganic hybrid perovskites have been studied in previous calculations and it would be meaningful to compare them with the present work. Note that the electronic structure near band edges and the vibrational spectrum of hybrid perovskites are similar to those of fully inorganic halide perovskites [14,23]. In Refs. [13,44], the room-temperature carrier mobility of

methylammonium lead iodide perovskite (MAPI) was calculated by considering the coupling between electrons and polar optical phonons. The former obtained 57 (40) cm^2/Vs for the electron (hole) mobility at carrier concentrations smaller than 10^{18} cm^{-3} using the Boltzmann transport theory, while the latter reported 133 (94) cm^2/Vs employing the Feynman polaron model. It should be noted that the SOC is lacking in the calculations of Filippetti *et al.* and, therefore, their mobility, particularly for the electron, is likely to be underestimated. Despite some inconsistency in the previous calculations, reported mobilities for MAPI are below the present results for $CsPbI_3$. This result implies that fully inorganic halide perovskites are beneficial over hybrid systems in terms of the carrier transport.

IV. CONCLUSION

In summary, we investigate the transport properties of $CsPbX_3$ using DFT calculations in conjunction with Boltzmann transport theory, considering the polar LO phonon scattering. The calculation of the scattering rates shows that the highest LO mode serves as the dominant scattering channel due to the larger electron-phonon coupling. The mobility turns out to be higher in $CsPbI_3$, followed by $CsPbBr_3$ and $CsPbCl_3$, which is explained by the differences in the effective mass and the scattering rates. Through the detailed analysis on the electronic and vibrational properties as well as the scattering rates due to their coupling, our results provide important insights into the role of halide species in the transport properties of $CsPbX_3$.

ACKNOWLEDGMENTS

This work is supported by the Fundamental Research Program (No. PNK5570) of the Korea Institute of Materials Science. S.H. acknowledges support from the Creative Materials Discovery Program through the National Research Foundation of Korea (NRF) funded by the Ministry of Science and ICT (Grant No. 2017M3D1A1040689).

[1] M. A. Green, A. Ho-Baillie, and H. J. Snaith, The emergence of perovskite solar cells, Nat. Photonics **8**, 506 (2014).

[2] S. D. Stranks and H. J. Snaith, Metal-halide perovskites for photovoltaic and light-emitting devices, Nat. Nanotechnol. **10**, 391 (2015).

[3] M. A. Green, Y. Hishikawa, W. Warta, E. D. Dunlop, D. H. Levi, J. Hohl-Ebinger, and A. W. Ho-Baillie, Solar cell efficiency tables (version 50), Prog. Photovolt. Res. Appl. **25**, 668 (2017).

[4] M. Kulbak, S. Gupta, N. Kedem, I. Levine, T. Bendikov, G. Hodes, and D. Cahen, Cesium enhances long-term stability of lead bromide perovskite-based solar cells, J. Phys. Chem. Lett. **7**, 167 (2015).

[5] J. Duan, Y. Zhao, B. He, and Q. Tang, High-purity inorganic perovskite films for solar cells with 9.72% efficiency, Angew. Chem. Int. Ed. **57**, 3787 (2018).

[6] E. M. Hutter, R. J. Sutton, S. Chandrashekar, M. Abdi-Jalebi, S. D. Stranks, H. J. Snaith, and T. J. Savenije, Vapour-deposited cesium lead iodide perovskites: Microsecond charge carrier lifetimes and enhanced photovoltaic performance, ACS Energy Lett. **2**, 1901 (2017).

[7] S. Dastidar, S. Li, S. Y. Smolin, J. B. Baxter, and A. T. Fafarman, Slow electron–hole recombination in lead iodide perovskites does not require a molecular dipole, ACS Energy Lett. **2**, 2239 (2017).

[8] H. Zhu, M. T. Trinh, J. Wang, Y. Fu, P. P. Joshi, K. Miyata, S. Jin, and X.-Y. Zhu, Organic cations might not be essential to the remarkable properties of band edge carriers in lead halide perovskites, Adv. Mater. **29**, 1603072 (2017).

[9] C. C. Stoumpos, C. D. Malliakas, J. A. Peters, Z. Liu, M. Sebastian, J. Im, T. C. Chasapis, A. C. Wibowo, D. Y. Chung, and A. J. Freeman *et al.*, Crystal growth of the perovskite semiconductor $CsPbBr_3$: A new material for high-energy radiation detection, Cryst. Growth Des. **13**, 2722 (2013).

[10] M. I. Saidaminov, M. A. Haque, J. Almutlaq, S. Sarmah, X.-H. Miao, R. Begum, A. A. Zhumekenov, I. Dursun, N. Cho, and B. Murali *et al.*, Inorganic lead halide perovskite single crystals: Phase-selective low-temperature growth, carrier transport properties, and self-powered photodetection, Adv. Opt. Mater. **5**, 1600704 (2017).

[11] X. Miao, T. Qiu, S. Zhang, H. Ma, Y. Hu, F. Bai, and Z. Wu, Air-stable $CsPb_{1-x}Bi_xBr_3$ $(0 \leq x \ll 1)$ perovskite crystals: Optoelectronic and photostriction properties, J. Mater. Chem. C **5**, 4931 (2017).

[12] H. Zhang, X. Liu, J. Dong, H. Yu, C. Zhou, B. Zhang, Y. Xu, and W. Jie, Centimeter-sized inorganic lead halide perovskite $CsPbBr_3$ crystals grown by an improved solution method, Cryst. Growth Des. **17**, 6426 (2017).

[13] J. M. Frost, Calculating polaron mobility in halide perovskites, Phys. Rev. B **96**, 195202 (2017).

[14] C. W. Myung, J. Yun, G. Lee, and K. S. Kim, A new perspective on the role of A-site cations in perovskite solar cells, Adv. Energy Mater. **8**, 1702898 (2018).

[15] K. Miyata, D. Meggiolaro, M. T. Trinh, P. P. Joshi, E. Mosconi, S. C. Jones, F. De Angelis, and X.-Y. Zhu, Large polarons in lead halide perovskites, Sci. Adv. **3**, e1701217 (2017).

[16] C. Motta and S. Sanvito, Electron–phonon coupling and polaron mobility in hybrid perovskites from first principles, J. Phys. Chem. C **122**, 1361 (2018).

[17] K. Krishnaswamy, B. Himmetoglu, Y. Kang, A. Janotti, and C. G. Van de Walle, First-principles analysis of electron transport in $BaSnO_3$, Phy. Rev. B **95**, 205202 (2017).

[18] Y. Kang, K. Krishnaswamy, H. Peelaers, and C. G. Van de Walle, Fundamental limits on the electron mobility of β-Ga_2O_3, J. Phys.: Condens. Matter **29**, 234001 (2017).

[19] G. Kresse and J. Furthmüller, Efficient iterative schemes for *ab initio* total-energy calculations using a plane-wave basis set, Phys. Rev. B **54**, 11169 (1996).

[20] G. Kresse and D. Joubert, From ultrasoft pseudopotentials to the projector augmented-wave method, Phys. Rev. B **59**, 1758 (1999).

[21] J. Heyd, G. E. Scuseria, and M. Ernzerhof, Hybrid functionals based on a screened coulomb potential, J. Chem. Phys. **118**, 8207 (2003).; Erratum: Hybrid functionals based on a screened coulomb potential [J. Chem. Phys. 118, 8207 (2003)], J. Chem. Phys. **124**, 219906 (2006).

[22] M. A. Becker, R. Vaxenburg, G. Nedelcu, P. C. Sercel, A. Shabaev, M. J. Mehl, J. G. Michopoulos, S. G. Lambrakos, N. Bernstein, and J. L. Lyons *et al.*, Bright triplet excitons in caesium lead halide perovskites, Nature **553**, 189 (2018).

[23] L. D. Whalley, J. M. Frost, Y.-K. Jung, and A. Walsh, Perspective: Theory and simulation of hybrid halide perovskites, J. Chem. Phys. **146**, 220901 (2017).

[24] J. Even, L. Pedesseau, J.-M. Jancu, and C. Katan, Importance of spin–orbit coupling in hybrid organic/inorganic perovskites for photovoltaic applications, J. Phys. Chem. Lett. **4**, 2999 (2013).

[25] K. Hummer, J. Harl, and G. Kresse, Heyd-scuseria-ernzerhof hybrid functional for calculating the lattice dynamics of semiconductors, Phys. Rev. B **80**, 115205 (2009).

[26] R. Wahl, D. Vogtenhuber, and G. Kresse, $SrTiO_3$ and $BaTiO_3$ revisited using the projector augmented wave method: Performance of hybrid and semilocal functionals, Phys. Rev. B **78**, 104116 (2008).

[27] A. Togo and I. Tanaka, First principles phonon calculations in materials science, Scr. Mater. **108**, 1 (2015).

[28] D. Trots and S. Myagkota, High-temperature structural evolution of caesium and rubidium triiodoplumbates, J. Phys. Chem. Solids **69**, 2520 (2008).

[29] G. S. Rohrer, *Structure and Bonding in Crystalline Materials* (Cambridge University Press, New York, 2001).

[30] A. Marronnier, H. Lee, B. Geffroy, J. Even, Y. Bonnassieux, and G. Roma, Structural instabilities related to highly anharmonic phonons in halide perovskites, J. Phys. Chem. Lett. **8**, 2659 (2017).

[31] R. X. Yang, J. M. Skelton, E. L. da Silva, J. M. Frost, and A. Walsh, Spontaneous octahedral tilting in the cubic inorganic cesium halide perovskites $CsSnX_3$ and $CsPbX_3$ (X = F, Cl, Br, I), J. Phys. Chem. Lett. **8**, 4720 (2017).

[32] D. Yang, J. Lv, X. Zhao, Q. Xu, Y. Fu, Y. Zhan, A. Zunger, and L. Zhang, Functionality-directed screening of Pb-free hybrid organic–inorganic perovskites with desired intrinsic photovoltaic functionalities, Chem. Mater. **29**, 524 (2017).

[33] P. Azarhoosh, S. McKechnie, J. M. Frost, A. Walsh, and M. Van Schilfgaarde, Research update: Relativistic origin of slow electron-hole recombination in hybrid halide perovskite solar cells, APL Mater. **4**, 091501 (2016).

[34] Y. Chang, C. Park, and K. Matsuishi, First-principles study of the structural and the electronic properties of the lead-halide-based inorganic-organic perovskites $(CH_3NH_3)PbX_3$ and $CsPbX_3$ (X = Cl, Br, I), J. Korean Phys. Soc. **44**, 889 (2004).

[35] J. M. Ziman, *Electrons and Phonons: The Theory of Transport Phenomena in Solids* (Oxford University Press, London, 1960).

[36] T.-H. Liu, J. Zhou, B. Liao, D. J. Singh, and G. Chen, First-principles mode-by-mode analysis for electron-phonon scattering channels and mean free path spectra in GaAs, Phys. Rev. B **95**, 075206 (2017).

[37] F. Giustino, Electron-phonon interactions from first principles, Rev. Mod. Phys. **89**, 015003 (2017).

[38] A. Link, K. Bitzer, W. Limmer, R. Sauer, C. Kirchner, V. Schwegler, M. Kamp, D. Ebling, and K. Benz, Temperature dependence of the E_2 and A_1(LO) phonons in GaN and AlN, J. Appl. Phys. **86**, 6256 (1999).

[39] R. Cuscó, E. Alarcón-Lladó, J. Ibanez, L. Artús, J. Jimenez, B. Wang, and M. J. Callahan, Temperature dependence of raman scattering in ZnO, Phys. Rev. B **75**, 165202 (2007).

[40] Z.-G. Yu, Rashba effect and carrier mobility in hybrid organic–inorganic perovskites, J. Phys. Chem. Lett. **7**, 3078 (2016).

[41] C. Verdi and F. Giustino, Fröhlich Electron-Phonon Vertex from First Principles, Phys. Rev. Lett. **115**, 176401 (2015).

[42] J. Kang and L.-W. Wang, High defect tolerance in lead halide perovskite $CsPbBr_3$, J. Phys. Chem. Lett. **8**, 489 (2017).

[43] L. M. Herz, Charge-carrier mobilities in metal halide perovskites: Fundamental mechanisms and limits, ACS Energy Lett. **2**, 1539 (2017).

[44] A. Filippetti, A. Mattoni, C. Caddeo, M. Saba, and P. Delugas, Low electron-polar optical phonon scattering as a fundamental aspect of carrier mobility in methylammonium lead halide $CH_3NH_3PbI_3$ perovskites, Phys. Chem. Chem. Phys. **18**, 15352 (2016).